Publ. Astron. Soc. Japan (2020) 72 (4), 68 (1–15)
doi: 10.1093/pasj/psaa051
Advance Access Publication Date: 2020 July 9

Optical and X-ray observations of stellar flares on an active M dwarf AD Leonis with the Seimei Telescope, SCAT, NICER, and OISTER

Kosuke Namekata,[1,*] Hiroyuki Maehara,[2] Ryo Sasaki,[3,4] Hiroki Kawai,[3] Yuta Notsu,[5,6] Adam F. Kowalski,[5,6] Joel C. Allred,[7] Wataru Iwakiri,[3,4] Yohko Tsuboi,[3] Katsuhiro L. Murata,[8] Masafumi Niwano,[8] Kazuki Shiraishi,[8] Ryo Adachi,[8] Kota Iida,[8] Motoki Oeda,[8] Satoshi Honda,[9] Miyako Tozuka,[9] Noriyuki Katoh,[9,10] Hiroki Onozato,[9] Soshi Okamoto,[1] Keisuke Isogai,[11] Mariko Kimura,[1,4] Naoto Kojiguchi,[1] Yasuyuki Wakamatsu,[1] Yusuke Tampo,[1] Daisaku Nogami,[1] and Kazunari Shibata[1,12]

[1]Department of Astronomy, Kyoto University, Kitashirakawa-Oiwake-cho, Sakyo, Kyoto, Kyoto 606-8502, Japan
[2]Okayama Branch Office, Subaru Telescope, National Astronomical Observatory of Japan, NINS, Kamogata, Asakuchi, Okayama 719-0232, Japan
[3]Department of Physics, Faculty of Science and Engineering, Chuo University, 1-13-27 Kasuga, Bunkyo-ku, Tokyo 112-8551, Japan
[4]Institute of Physical and Chemical Research (RIKEN), 2-1 Hirosawa, Wako, Saitama 351-0198, Japan
[5]Laboratory for Atmospheric and Space Physics, University of Colorado Boulder, 3665 Discovery Drive, Boulder, CO 80303, USA
[6]National Solar Observatory, 3665 Discovery Drive, Boulder, CO 80303, USA
[7]NASA/Goddard Space Flight Center, Code 671, Greenbelt, MD 20771, USA
[8]Department of Physics, Tokyo Institute of Technology, 2-12-1 Ookayama, Meguro-ku, Tokyo 152-8551, Japan
[9]Nishi-Harima Astronomical Observatory, Center for Astronomy, University of Hyogo, Sayo, Sayo, Hyogo 679-5313, Japan
[10]Graduate School of Human Development and Environment, Kobe University, 3-11 Tsurukabuto, Nada-ku, Kobe, Hyogo 657-8501, Japan
[11]Okayama Observatory, Kyoto University, 3037-5 Honjo, Kamogatacho, Asakuchi, Okayama 719-0232, Japan
[12]Astronomical Observatory, Kyoto University, Kitashirakawa-Oiwake-cho, Sakyo, Kyoto, Kyoto 606-8502, Japan

*namekata@kusastro.kyoto-u.ac.jp

Received 2020 March 28; Accepted 2020 May 8

Abstract

We report on multi-wavelength monitoring observations of an M-dwarf flare star AD Leonis with the Seimei Telescope (6150–7930 Å), SCAT (Spectroscopic Chuo-university Astronomical Telescope; 3700–7500 Å), and NICER (Neutron Star Interior Composition Explorer; 0.2–12.0 keV), with the collaboration of the OISTER (Optical and

Infrared Synergetic Telescopes for Education and Research) program. Twelve flares are detected in total, including ten Hα, four X-ray, and four optical-continuum flares; one of them is a superflare with a total energy of $\sim 2.0 \times 10^{33}$ erg. We found that: (1) during the superflare, the Hα emission line full width at 1/8 maximum dramatically increases to 14 Å from 8 Å in the low-resolution spectra ($R \sim 2000$) accompanied by large white-light flares, (2) some weak Hα/X-ray flares are not accompanied by white-light emissions, and (3) the non-flaring emissions show clear rotational modulations in X-ray and Hα intensity in the same phase. To understand these observational features, one-dimensional hydrodynamic flare simulations are performed using the RADYN code. We find the simulated Hα line profiles with hard and high-energy non-thermal electron beams to be consistent with the initial phase line profiles of the superflares, while those with a softer and/or weak-energy beam are consistent with those in decay phases, indicating the changes in the energy fluxes injected to the lower atmosphere. Also, we find that the relation between the optical continuum and Hα intensity is nonlinear, which can be one cause of the non-white-light flares. The flare energy budget exhibits diversity in the observations and models, and more observations of stellar flares are necessary for constraining the occurrence of various emission line phenomena in stellar flares.

Key words: stars: activity — stars: coronae — stars: flare — stars: magnetic fields — starspots

1 Introduction

Solar flares are abrupt brighteningson the solar surface. During flares, magnetic energy stored around sunspots is believed to be converted to kinetic and thermal energies through magnetic reconnection in the corona (see Priest 1981; Shibata & Magara 2011; and references therein). In the standard scenario, the released energies are transported from the corona to the lower atmosphere by non-thermal high-energy particles and thermal conduction. The energy injection causes chromospheric evaporations and chromospheric condensations, producing bright coronal and chromospheric emissions, respectively. In this context, these chromospheric/coronal emissions have information on the accelerated particles in the reconnection site, which can give us a clue to understanding the unknown acceleration mechanism of the non-thermal particles.

As expected from a solar analogy, stellar flares are often observed in radio, visible, and X-ray ranges similar to solar flares. In particular, magnetically active stars, such as young T-tauri stars (e.g., Koyama et al. 1996; Benz & Güdel 2010) and M-type stars (e.g., Hawley & Pettersen 1991; Kowalski et al. 2013), often show large flares, called superflares. The superflares release much larger total energies (10^{33}–10^{38} erg) than the maximum solar flares ($\sim 10^{32}$ erg). This kind of extreme event on stars has been getting more and more attention in terms of exoplanet habitability around active young stars (Segura et al. 2010; Airapetian et al. 2016; Lingam & Loeb 2017) and a possible extreme event on the Sun (Aulanier et al. 2013; Shibata et al. 2013; Hayakawa et al. 2017).

As solar flare dynamics are well understood thanks to multi-wavelength observations, the understanding of large stellar flares is also expected to be deepened by such observations. More samples are required to reveal the universality and diversity of solar and stellar flares. Magnetically active M dwarfs are among the best targets for flare monitoring, as their flares are observed from X-ray to radio. In particular, stellar flares produce greatly enhanced emission in chromospheric lines, such as the hydrogen Balmer series, Ca II H and K, which are observable from the ground. The hydrogen lines tend to have a relatively fast rise phase, but the peak is often delayed compared to the continuum emission (Kahler et al. 1982; Hawley & Pettersen 1991). The radiated energy in hydrogen lines is relatively small compared to the continuum (Hawley & Pettersen 1991). Balmer line broadening up to 20 Å has been observed during stellar flares (Hawley & Pettersen 1991), which is interpreted as non-thermal broadening or Stark (pressure) broadening. Recent numerical simulation shows that the broadenings of the higher-order Balmer lines (e.g., Hγ) are good tools to estimate the chromospheric density, which can be a clue to the injected accelerated particles (Allred et al. 2006; Paulson et al. 2006; Kowalski et al. 2017). However, in almost all studies, the temporal evolution of the Balmer line widths has not been well investigated, although the flaring atmosphere dramatically changes during flares. Moreover, the energy budget for each wavelength is not confirmed for stellar flares, although it is known that there is diversity even in solar flares.

In this paper we report on the optical and X-ray monitoring observation of an M-dwarf flare star AD Leo during 8.5 nights by the Seimei–OISTER campaign to reveal the features of stellar flares. In this campaign, we mainly used a low-resolution spectrograph on the 3.8 m Seimei Telescope (Kurita et al. 2020). We also conducted optical spectroscopy and photometric observations with the help of the OISTER (Optical and Infrared Synergetic Telescopes for Education and Research)[1] program and with the Spectroscopic Chuo-university Astronomical Telescope (SCAT) at Chuo University. We also obtained the X-ray monitoring data from NICER (Neutron Star Interior Composition Explorer) during this observational period. In section 2 we review observations and analyses. In section 3 we introduce features of the observed stellar flares. In section 4 we show the rotational modulations of AD Leo. In section 5 we perform one-dimensional hydrodynamic simulations of stellar flares to understand the flare properties. Finally, we discuss the observations and numerical simulations in section 6.

2 Observations and data reduction

2.1 Target star

In 2019, we carried out extensive campaign monitoring observations on the nearby M dwarf AD Leo (GJ 388). AD Leo is classified as a dMe 3.5 star (Shkolnik et al. 2009), whose distance from the Earth is about 4.9 pc. Frequent stellar flares have been observed on AD Leo in several wavelength ranges (Hawley et al. 1995, 2003; Kowalski et al. 2013), and an extremely large superflare has also been observed (Hawley & Pettersen 1991). The flare occurrence frequency is reported to have a power-law distribution, causing 0.76 flares per day (Pettersen et al. 1984).

2.2 Spectral data

We mainly used the Seimei Telescope located at Okayama Observatory, Japan, for spectroscopic data. The Seimei Telescope is a 3.8 m optical and infrared telescope (Kurita et al. 2020). We used the KOOLS-IFU instrument (Matsubayashi et al. 2019), which is a low-resolution spectrograph (KOOLS) with an optical-fiber integral field unit (IFU), on the Nasmyth focus. The grism we used covers 6150 to 7930 Å, and the spectral resolution (R) is ~2000. We conducted 8.5 nights of spectroscopic monitoring observation of AD Leo with Seimei Telescope/KOOLS-IFU from 2019 March to April (table 1). The time resolutions are 42 or 72 s, including the 12 s read-out time to achieve a signal-to-noise ratio ~100. The KOOLS-IFU produces two-dimensional spectroscopic data, and we used only the fiber array where the stellar integrated brightness was more than 50% of that of the maximum fiber. Data reduction was done using the IRAF[2] package, PyRAF[2] software, and the data reduction packages developed by Matsubayashi et al. (2019).[3]

During this observational period of the Seimei Telescope we also conducted monitoring observations of the Balmer lines of AD Leo with the SCAT optical telescope, which is mounted on a building in the Korakuen campus of Chuo University in Japan. It consists of a MEADE 36 cm diameter telescope and an ATIK 460EX charge-coupled device (CCD) camera with a Shelyak Alpy 600 spectrometer. The spectrometer covers 3700 to 7500 Å, and the spectral resolution, R, is 600. About 600 s exposure was required to get a signal-to-noise ratio of >100. We executed the data reduction using the twodspec package of the IRAF software in the standard manner (dark subtraction, flat fielding, spectral extraction, sky subtraction, and wavelength calibration).

In the OISTER program, the spectroscopic observations were carried out with the Nayuta 2 m telescope at the Nishi-Harima Astronomical Observatory for two days (table 1). The MALLS (Medium And Low-dispersion Long-slit Spectrograph) was used with a resolving power (R) of ~10000 at 6500 Å, covering 6350–6800 Å. We aimed to use this instrument to detect line asymmetries of the Balmer lines (e.g., Honda et al. 2018), but the changes in the Hα profiles were too small, and significant line asymmetries were not detected.

2.3 Photometric data

In the OISTER program, time-resolved photometry was performed during this period by using the MITSuME 50 cm telescope at Okayama Observatory and the 40 cm telescope at Kyoto University. The MITSuME 50 cm telescope can acquire g'-, R_C-, and I_C-band images simultaneously by using two dichroic mirrors and three CCD cameras (Kotani et al. 2005). We described the observational log of MITSuME in table 1. Note that although the location is the same as that of the Seimei Telescope, the photometry has better sensitivity than the spectroscopy of Seimei. The CCDs of MITSuME have deteriorated recently, and the photometric sensitivity has become worse if we divide the images by flat frames. Therefore, most flares except for one large superflare could not be detected by MITSuME photometry even in the g'-band where flare amplitude is expected to be the largest among the three bands of MITSuME. Also, B-band photometric observations on AD Leo were conducted by the

1 ⟨http://oister.kwasan.kyoto-u.ac.jp/⟩.

2 IRAF and PyRAF are distributed by the National Optical Astronomy Observatories, which are operated by the Association of Universities for Research in Astronomy, Inc., under a cooperation agreement with the National Science Foundation.

3 ⟨http://www.kusastro.kyoto-u.ac.jp/kazuya/p-kools/reduction-201806/index.html⟩.

Table 1. Observing log.

Telescope/instrument (Data type)	UT Date (JD)	Time (hr)	Exp. time (s)	Flare #
Spectroscopy				
3.8 m Seimei/KOOLS-IFU	2019 Mar 22 (2458565)	2.6	60	1
(5000–8000 Å; $R \sim 2000$)	2019 Mar 23 (2458566)	4.6, 1	30	—
	2019 Mar 24 (2458567)	4.1	60	2, 3
	2019 Mar 25 (2458568)	2.5	30, 60	—
	2019 Mar 26 (2458569)	7.3	30	4, 5
	2019 Mar 27 (2458570)	5.1	30	6
	2019 Apr 12 (2458586)	5.9	30	7, 8, 9, 10
2 m Nayuta/MALLS (OISTER)	2019 Mar 24 (2458567)	5	120	2, 3
(6350–6800 Å; $R \sim 10000$)	2019 Mar 26 (2458569)	5	120	4, 5
36 cm SCAT	2019 Mar 23 (2458566)	2.5	600	
(3520–8040 Å; $R \sim 600$;	2019 Mar 24 (2458567)	4.5	600	2, 3
covering Hα, Hβ, Hγ, and Hδ)	2019 Mar 26 (2458569)	5.5	600	4, 5
	2019 Mar 27 (2458570)	2.5	600	
Photometry				
50 cm MITSuME (OISTER)	2019 Mar 22 (2458565)	6.9	5	1
($g'/R_C/I_C$-band photometry)†	2019 Mar 23 (2458565)	6.0	5	
	2019 Mar 24 (2458567)	6.8	5	—*
	2019 Mar 25 (2458568)	4.8	5	
	2019 Mar 26 (2458569)	7.0	5	—*
	2019 Mar 28 (2458571)	7.0	5	
	2019 Apr 11 (2458585)	4.5	5	
	2019 Apr 12 (2458586)	4.5	5	—*
	2019 Apr 13 (2458587)	4.6	5	
40 cm KU Telescope (OISTER)	2019 Apr 12 (2458586)	5	10	7, 9, 10
(B-band photometry)†				
X-ray				
ISS/NICER	2019 Mar 22–28 (2458565-71)	$\sim 0.5 \times 26$	—	4
(0.2–12 keV X-ray)	2019 Apr 11–13 (2458585-87)	$\sim 0.5 \times 10$	—	8, 11, 12

*There were observations when flares were detected by the Seimei Telescope and other telescopes, but no flares were detected by MITSuME.
†The g'-, R_C-, I_C-, B-band filter is a broad-band (full width ~1000 Å) one whose central wavelengths are 4858, 6588, 8060, 4448 Å, respectively.

40 cm telescope at Kyoto University only on 2019 April 12; the data are shown in the Appendix.

2.4 X-ray data

NASA's NICER (Gendreau et al. 2016) conducted monitoring observations on AD Leo during this period. NICER is the soft X-ray instrument onboard the International Space Station, and observed AD Leo for about 1 ks for each orbital period of ISS (about 90 min). The observation was carried out several times during each night. NICER is not an imaging instrument, so background spectra must be subtracted to get the stellar spectra. The data were processed using the NICER software version 2019-10-30, which can estimate the background spectra at a given NICER observational orbit.[4]

In making the light curves, we used the 0.5–8 keV band corresponding to channels 50 through 800. Below channel ~50 and above ~800 there is optical contamination due to the ambient light. For two flares clearly detected by NICER (flares #4 and #12), we also analyzed X-ray spectra in the flare phases. The integrated times are indicated by the error bars of the derived emission measure (EM) and temperature as in figure 6. We fitted the pre-flare subtracted X-ray spectra (0.5–8.0 keV) with a simple thin-thermal model of single-temperature plasma where the abundance ratios of heavy elements are fixed to solar values (e.g., Tsuboi et al. 2016). We derived the emission measures, temperatures, and radiation flux by using the apec models in XSPEC as installed in HEASoft;[5] the parameters are summarized in table 2.

4 ⟨https://heasarc.gsfc.nasa.gov/docs/nicer/tools/nicer_bkg_est_tools.html⟩.

5 ⟨https://heasarc.gsfc.nasa.gov/xanadu/xspec/⟩.

Table 2. X-ray spectral best-fit parameters for flare #4.

Parameters	Time 1	Time 2	Time 3
$N_{\rm H}$ [10^{20} cm^{-2}]	3.48	8.50	5.23
kT [keV]	2.62	1.31	1.27
norm	8.14×10^{-2}	5.07×10^{-2}	3.10×10^{-2}

2.5 Emission line/continuum fluxes

Emission fluxes were calculated for the hydrogen Balmer lines (Hα, Hβ, Hγ, Hδ), and the He I line 6678.15 Å, and the g'-, $R_{\rm C}$-, and $I_{\rm C}$-band continuum. For the emission lines, the flux ($F_{\rm line}$) is calculated from the equivalent width (EW) and the local continuum enhancement levels ($F_{\rm flare}/F_{\rm pre\text{-}flare}$), and the local continuum enhancement level is calculated based on the g' band and $R_{\rm C}$ bands (cf. the appendix of Hawley & Pettersen 1991). First, the synthetic g'-band flux, $R_{\rm C}$-band flux, and local continuum flux ($F_{\rm local\text{-}cont.}$) at each emission line in quiescence is calculated based on the flux-calibrated AD Leo spectra taken by SCAT. Second, the local-continuum enhancement levels at each line (i.e., $F_{\rm flare}/F_{\rm pre\text{-}flare}$) is calculated based on the g'- and $R_{\rm C}$-band enhancement levels obtained from photometry. Finally, the line emission flux is calculated from the equivalent width and local continuum enhancement levels (i.e., $F_{\rm line} = {\rm EW} \times F_{\rm flare}/F_{\rm pre\text{-}flare} \times F_{\rm local\text{-}cont.}$). The H$\alpha$ and He I line 6678.15 Å refer to the $R_{\rm C}$-band flux, and the others to the g'-band flux. The fluxes of line emissions can have errors because of the contamination of line emissions by broad-band continuum fluxes. However, as for flare #1, for example, the effect would be less effective because the enhancement of equivalent width was 10 Å at most, while the continuum bands have >100% enhancement in ∼1000 Å bandwidth.

3 Flare atlas: Light curves and spectra

3.1 Observational summary

We carried out the monitoring observations on AD Leo for 8.5 d, and the clear-sky ratio was about 50%. Figure 1 indicates the overall light curve during this campaign. Twelve flares were detected by eye, mainly with the Hα monitoring with Seimei/KOOLS-IFU (see table 1), although there could be a larger number of small flares which could not be identified by eye. The Balmer lines show emission even in quiescence, indicating very high atmospheric heating. The Hα equivalent width in quiescence is about −3.5 Å, and the enhancement during flares is typically 1–1.5 Å. Only one flare (flare #1) shows very high enhancement of Hα (∼10 Å). The number of flares detected by Balmer lines is 10. Even though the simultaneous photometry is limited, four of them are clearly detected by optical photometry, while five of them did not clearly show white-light emissions (one of them has no photometry). Four of them are also detected by higher-resolution spectroscopy with Nayuta/MALLS, but are too weak to identify clear line asymmetry like Honda et al. (2018). Two of them are detected by the NICER X-ray detector. The count rate of 0.5–8.0 keV in quiescence is about 18 counts s^{-1}. Also, two additional flares are detected by NICER X-ray, although there are no clear Hα observations (flares #11, #12). In the following subsections we show the typical and prominent stellar flares detected

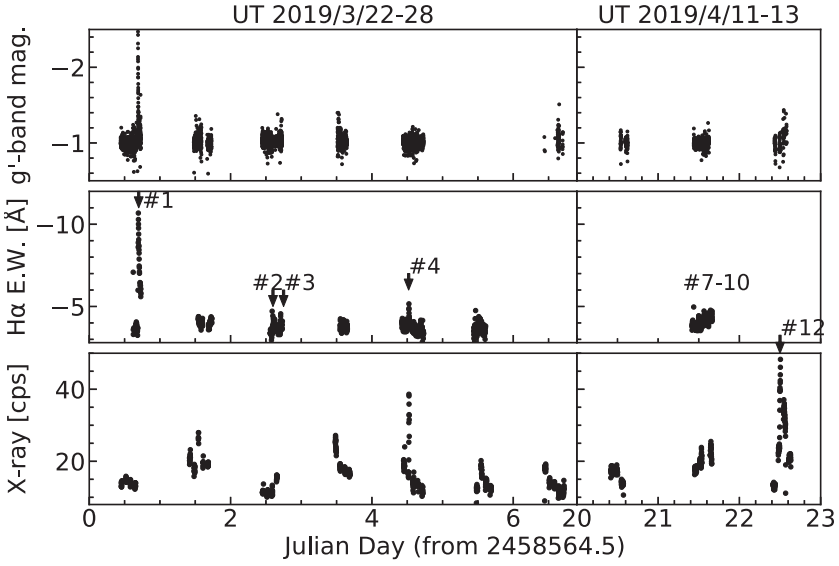

Fig. 1. Overall light curves of AD Leo during this campaign observation. Top: Light curve in g'-band magnitude. Middle: Hα equivalent width. Bottom: X-ray count rates [counts s^{-1}] in 0.5–8 keV.

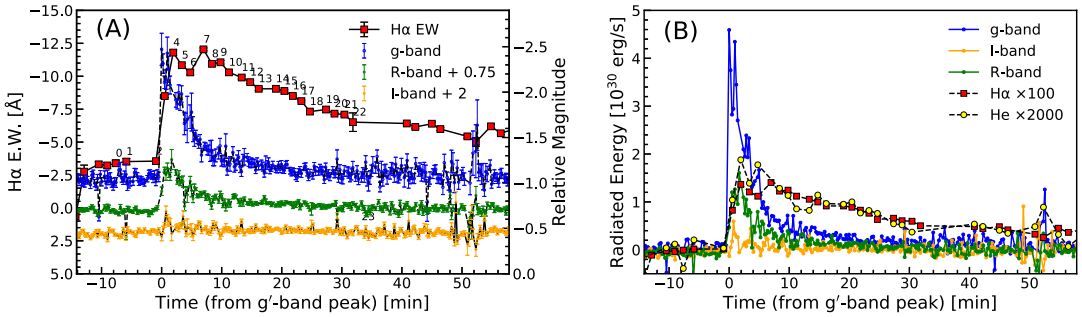

Fig. 2. (A) Light curve of flare #1 observed by Seimei Telescope/KOOLS-IFU (Hα) and MITSuME (g', R_C, I_C). The equivalent width is corrected by the continuum enhancements. (B) Light curve of flare #1 in units of erg s^{-1}. (Color online)

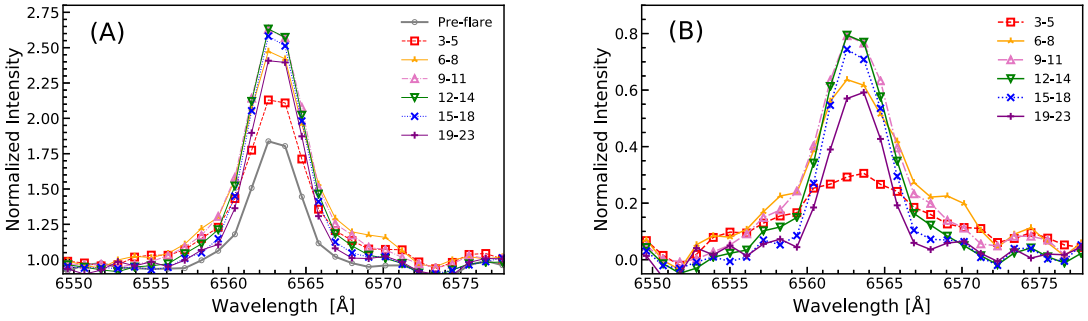

Fig. 3. (A) Hα spectra during flare #1. The numbers described in the legend are the same as in figure 2. We combined three to five spectra to make the spectra in this panel. (B) Pre-flare subtracted spectra of flare #1. (Color online)

(flares #1, #2, #3, and #4); all the other flares are shown in the Appendix.

3.2 Flare #1: A superflare showing large line broadening

Figure 2 shows the light curve of flare #1 observed by Seimei spectroscopy and MITSuME photometry. Unfortunately, there were no X-ray observations during this flare. Panel (A) shows that the equivalent width of Hα becomes -12 from -3.5 Å. The g'-band continuum becomes four times brighter than the quiescence, and the contrast is largest among the three filters. This can indicate very blue spectra of white-light continuum emissions, but M dwarfs are also very red, so a flat spectrum leads to larger flux enhancements as well. Panel (B) shows the temporal evolution of the radiated flux for each wavelength. The energies radiated in the continuum bands are much larger than the line emissions. The total radiated energies (and ratios relative to the g-band energy) in the g'-band, R_C-band, and I_C-band continuum, Hα, and He lines are calculated to be 1.4×10^{33} erg, 4.7×10^{32} erg (0.34), 7.0×10^{31} erg (0.05), 2.5×10^{31} erg (0.018), and 1.3×10^{30} erg (0.0093), respectively, and the flare is classified to be a superflare (a flare with a total energy of more than 10^{33} erg, $\sim$10 times more energy than the largest scale of solar flares; Maehara et al. 2012). Here, to calculate the flare energies, the flare fluxes in continuum and line emission in figure 2(B) were time-integrated between -2.6 min and 36 min and between -2.6 min and 58 min, respectively. Because the observations finished before the Hα and He line flare emissions completely decayed, the energies of the line emissions would be underestimated to some extent. The duration of the Hα flare is more than 1 hr, while the white-light flares lasted about 15 min. The continuum fluxes have shorter durations than the chromospheric line emission, which can be an indication of the Neupert effect in the case of solar flares (Neupert 1968). The color temperature of the white-light emission during the flare is calculated to be typically 14000^{+17000}_{-8000} K if we assume black-body radiation for the g'-band and R-band fluxes. Note that the continuum flux ratio was very noisy during the flare, so the error bar of the emission temperature is very large. The temporal evolution of the white-light emission temperature is therefore not significantly found. However, it has been reported that broad-band continua, especially g'-band, could be affected by emission lines (e.g., Kowalski et al. 2019), so we need to be careful about the interpretation of the emission temperatures derived here.

Figure 3 shows the temporal evolution of the low-resolution Hα spectra during these flares. Panel (A) shows the spectra normalized by the continuum level, and

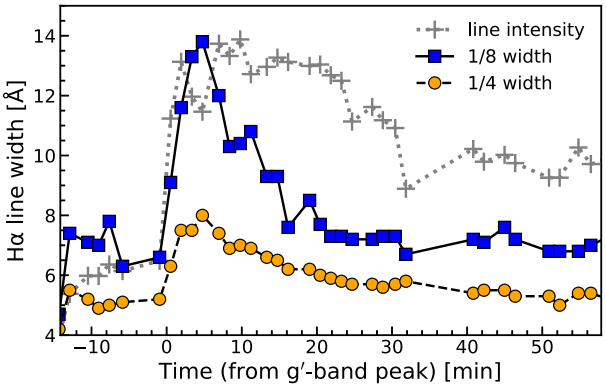

Fig. 4. Temporal evolution of the Hα line width and line intensity of flare #1. Open squares and open circles indicate the line width where the line intensity is 1/8 and 1/4 of the peak intensity, respectively. The gray crosses are the scaled line peak intensity. (Color online)

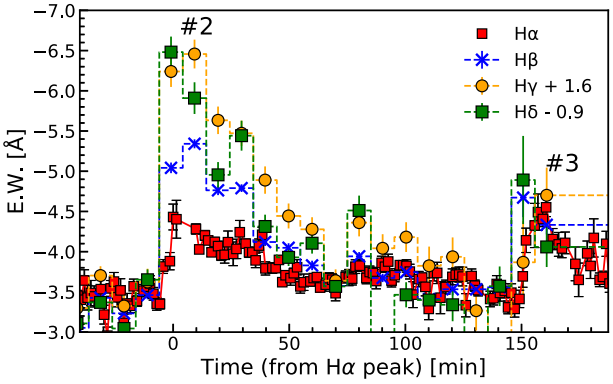

Fig. 5. Equivalent width of Balmer lines during flares #2 and #3 observed by the Seimei Telescope and SCAT. The relative values are corrected and the pre-flare levels are set to be the same value. (Color online)

panel (B) the pre-flare subtracted spectra. First, we could not find any line asymmetry during this flare, although blue and red asymmetries are frequently observed during not only stellar flares but also solar flares (e.g., Ichimoto & Kurokawa 1984; Tei et al. 2018; Honda et al. 2018; Muheki et al. 2020). Second, we found significant line-wing broadenings of the Hα line during the flare, as you can see in figure 3(B). The line broadening is especially prominent in the initial phase of the flare, but it is not prominent in the later decay phase. Figure 4 shows the temporal evolution of the line width and line peak intensity. As you can see, both line width and intensity largely increase in the initial phase of the flare when the white-light emissions are seen. In the decay phase, the line width dramatically decreases while the line peak intensity does not change much.

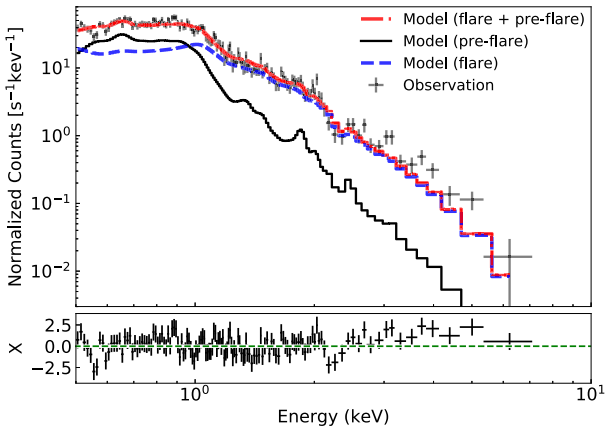

Fig. 6. Light curves of flare #4 observed in the *g* band [MITSuME, panel (a)], Balmer lines [Seimei Telescope and SCAT, panel (b)], and X-ray [NICER, panel (c)]. Panel (d) shows time variations of the emission measure and temperature during the flare. The values are derived from the pre-flare subtracted X-ray spectra (0.5–8.0 keV). (Color online)

3.3 Flares #2 and #3: A flare showing clear Balmer line decay

Figure 5 shows the light curves of flares #2 and #3, observed by Seimei/KOOLS-IFU and SCAT. There were photometric observations by MITSuME during this flare, but no significant white-light enhancement can be seen. The equivalent width change of the higher-level Balmer lines (e.g., Hδ and Hγ) is larger than the lower-level (e.g., Hα), which would be because there is a lower continuum in the blue. However, the decay timescales for each line are quite similar. The decay timescale for each Balmer line is not easy to interpret, because temperature, density, and the difference in opacity for each line contribute to it.

3.4 Flare #4: A small flare observed by all the instruments

Figure 6 shows the light curve of flare #4, and there are observations by all instruments (Seimei/KOOLS-IFU, SCAT, Nayuta/MALLS, MITSuME, and NICER) during the flare. Enhancement of Balmer lines and X-ray are clearly detected, but the continuum emissions are too weak to detect with the MITSuME photometric sensitivity.[6] The enhancement of the equivalent width is the same for all Balmer lines, which is different from flare #2, although the enhancement level is similar. The total radiated energy in Hα, Hβ, Hγ, and Hδ are calculated to be 1.1×10^{30} erg, 1.6×10^{30} erg, 5.0×10^{29} erg, and 9.6×10^{29} erg, respectively.

6 As we described, the MITSuME CCDs have the inevitable noise pattern, and the flat framing can make the photometric sensitivity worse.

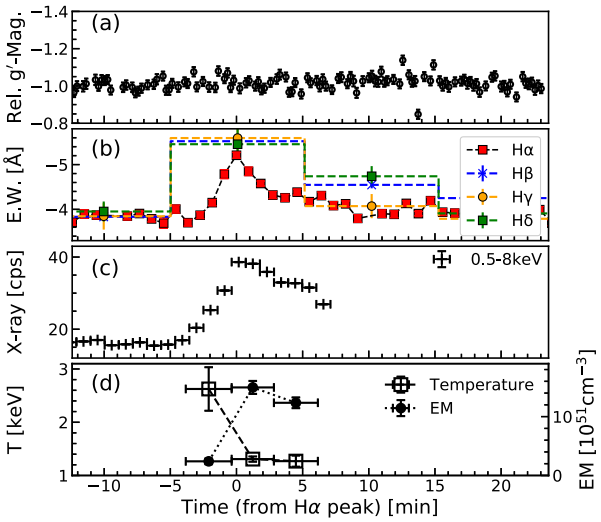

Fig. 7. X-ray spectra (0.5–10 keV) at the peak of flare #4. The gray crosses indicate the X-ray spectrum observed by NICER. The red dash-dotted line indicates the model spectra obtained by fitting the observation with a simple thin-thermal model (the apec model in XSPEC). The black solid line is the pre-flare spectra, and the blue dashed line indicates the flare-only spectra (i.e., the red line minus the black line). As a result of the model fitting, the reduced chi-squared is 1.23. The bottom panel indicates values of X = (data − model)/error (normalized by one sigma) for each bin. (Color online)

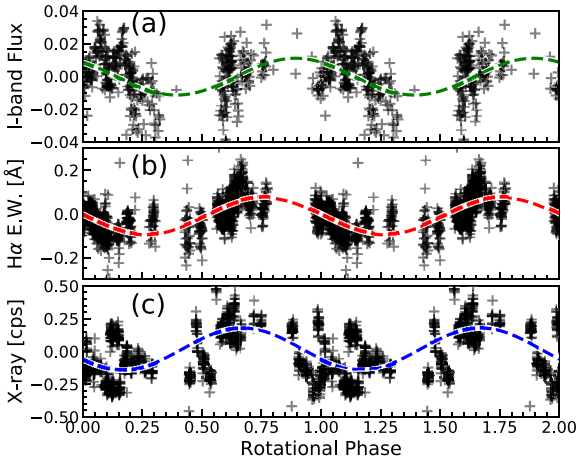

Fig. 8. Light curves relative to the mean value of (a) *I*-band continuum, (b) Hα, and (c) soft X-ray folded by the rotational period of ∼2.24 d. Note that flares were removed from the panel. Two rotational phases are plotted. The dotted line in each panel indicates the best-fitting sinusoidal curve. (Color online)

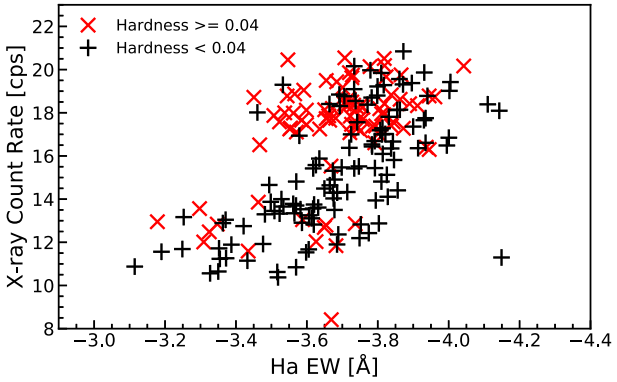

Fig. 9. Comparison between Hα equivalent width and X-ray count rates (0.5–8 keV) during a non-flaring phase. The red pluses and black crosses show the values where the hardness ratio values [i.e., *F*(2–8 keV)/*F*(0.5–2 keV)] are <0.04 and >0.04, respectively. (Color online)

For the X-ray data, the rise, peak, and initial decay phase were successfully observed. The count rates become about twice the quiescent values. The results of the model fitting of the flare spectra are also plotted in panel (d) of figure 7. The emission measure and temperature at the flare peak are derived as 1.15×10^{52} cm^{-3} and 1.57 keV (18.2 MK), respectively. After the temperature increases initially, the emission measure increases later, which is similar to the typical X-ray behavior accompanied with chromospheric evaporations in solar flares (e.g., Shibata & Yokoyama 2002). The observed X-ray flare energy in 0.5–10 keV is calculated to be 3.4×10^{31} erg, which is larger by about one order of magnitude than the Balmer line energy. Note that even in the initial phase, no significant hard X-ray power-law component is detected and the spectra can be fitted with only the single-component thermal spectra.

4 Rotational modulation

Figure 8 shows the light curves folded with the rotational period of 2.2399 d reported by Hunt-Walker et al. (2012). We removed the visibly checked flares to make figure 8. The Hα and X-ray phase-folded light curves show a clear periodic feature, which would be the signature of the rotational modulations of AD Leo with the bright active region in the chromosphere and corona. On the other hand, the photometric light curves do not show clear periodicity, probably due to the lack of photometric sensitivity. The phase-folded light curves are fitted with the simple sinusoidal curve indicated with the dotted lines. The phase difference between X-ray and Hα is only 0.094, and that between X-ray and *I*-band continuum is 0.22. Although the *I*-band periodicity is not clear, the phase of the X-ray and Hα periodicity seems to be highly correlated.

Figure 9 shows a comparison between X-ray and Hα intensity where both data exist at the same time. The X-ray and Hα intensity have a positive correlation, while there looks to be no correlation between them for the high hardness ratio. The amplitude of the X-ray modulations (16%) is twice that of the Hα modulation (8%), which may be caused by the filling factor or contrast of the active regions.

5 Radiative-hydrodynamic flare modeling

In section 3 we found that (1) accompanied by the large white-light enhancement, the Hα emission line width dramatically increases to 14 Å from 8 Å, and that (2) some weak Hα flares are not accompanied by white-light emission. These observational features motivate us to carry out numerical modeling of stellar flares to find out what happens in the atmosphere. In this section we report the results of one-dimensional radiative-hydrodynamic (RHD) flare modeling with the RADYN code (Carlsson & Stein 1992, 1995, 1997, 2002), which calculates hydrogen, helium, and Ca II in a non-LTE framework and with non-equilibrium ionization/excitation. We refer the reader to Allred, Kowalski, and Carlsson (2015) and (Kowalski et al. 2015, 2017) for extensive descriptions of the flare simulations.

5.1 RADYN flare model setup

The pre-flare atmosphere ($\log g = 4.75$) for an M dwarf in our modeling is described in Appendix A of Kowalski et al. (2017). The pre-flare coronal electron density becomes up to 10^{11} cm^{-3}. Although this value is larger by one or two orders of magnitude than that of the solar atmosphere, it is approximately consistent with the stellar X-ray observations (e.g., Osten et al. 2006).

Several improvements have been made to the RADYN flare code since Allred, Kowalski, and Carlsson (2015), which are worth noting here (they will be described further in A. F. Kowalski in preparation). The hydrogen broadening from Kowalski et al. (2017) and Tremblay and Bergeron (2009) has been included in the dynamic simulations; since we are comparing to Hα observations, this update to the hydrogen broadening is a critical improvement (A. F. Kowalski in preparation). The pre-flare atmosphere was relaxed with this new hydrogen broadening, and we choose to use the X-ray backheating formulation from Allred et al. (2005) for these models (A. F. Kowalski in preparation); the resulting pre-flare apex temperature is $\sim$3 MK, with electron density $\sim 10^{11}$ cm^{-3}. Finally, we used a new version of the F-P solver (A. F. Kowalski in preparation), which gives a moderately smoother electron beam energy deposition profile over height in the upper chromosphere. These changes have been implemented for the solar flare models presented in Graham et al. (2020).

Recently, this kind of RHD simulation has been widely carried out for the modeling of solar flares and dMe flares. However, the Hα behavior has not been so well investigated, partly because it is difficult to understand due to its non-LTE formation properties and large opacity variations over the line profile. In this study we revisit the basic properties of the Hα lines for dMe flares, and our aim in the numerical simulation is (1) to understand the Hα line width behaviors as a function of the injected energy, and (2) to understand the basic relation between Hα and the optical continuum.

5.2 Flare heating inputs

In this subsection we introduce the flare heating parameters used in our simulations. We aim to know the Hα/continuum intensity and Hα line width as a response to the flare heatings. We performed two kinds of simulations in which lower atmospheres are heated by (i) the non-thermal high-energy electrons (e.g., Kowalski et al. 2017) and (ii) thermal conduction from the heated loop top (e.g., Fisher 1989; Hori et al. 1997; Kowalski et al. 2017). We performed the non-thermal and thermal simulations separately to see the difference in the behavior of the emission atmosphere. Note that we consider only a one-dimensional tube in this study, but non-thermal line broadening among multi-loops (e.g., Fuhrmeister et al. 2011) may also have to be considered in the future (e.g., Warren 2006; Kowalski et al. 2017).

In the case of non-thermal heating, the energy flux density of non-thermal electrons with a power-law profile [$F(E) \propto E^{-\delta}$] is injected from the loop top. The important parameters are the total energy flux density ($F_{\rm NT}$), the lower energy cutoff ($E_{\rm C}$), and the power-law index (δ). Again, we aim to know the Hα/continuum intensity and line width by controlling these parameters. For simplicity, $E_{\rm C}$ is chosen to be 37 keV (Allred et al. 2015). $F_{\rm NT}$ is chosen to be 10^{10} erg cm^{-2} s^{-1} (F10), 10^{11} erg cm^{-2} s^{-1} (F11), 10^{12} erg cm^{-2} s^{-1} (F12; hereafter, we express the flare model with $F_{\rm NT}$ of 10^{10} erg cm^{-2} s^{-1} as F10), following the values simulated in previous works for large solar flares (Holman et al. 2003; Allred et al. 2005, 2006; Kowalski et al. 2015), and the power-law index δ is determined to be 3 and 5. The heating profile is assumed to be a triangle time variation with a peak time of 2 s, where the energy flux linearly increases and decreases in the rising and decay phase, respectively.

For thermal-conduction heating, the heating source term is input to the energy equation at the magnetic loop top (e.g., Hori et al. 1997). The energy flux of the thermal source is 5×10^{10} erg cm^{-2} s^{-1} (5F10), 10^{11} erg cm^{-2} s^{-1} (F11), 5×10^{11} erg cm^{-2} s^{-1} (5F11), and 10^{12} erg cm^{-2} s^{-1} (F12) per each magnetic loop. The heating profile is also a triangle time variation with a peak time of 4 s, which is twice the non-thermal case.

5.3 Simulation result I: Hα line broadening for non-thermal/thermal heating

In this subsection we show the Hα line broadening for the non-thermal/thermal heatings as a response to different

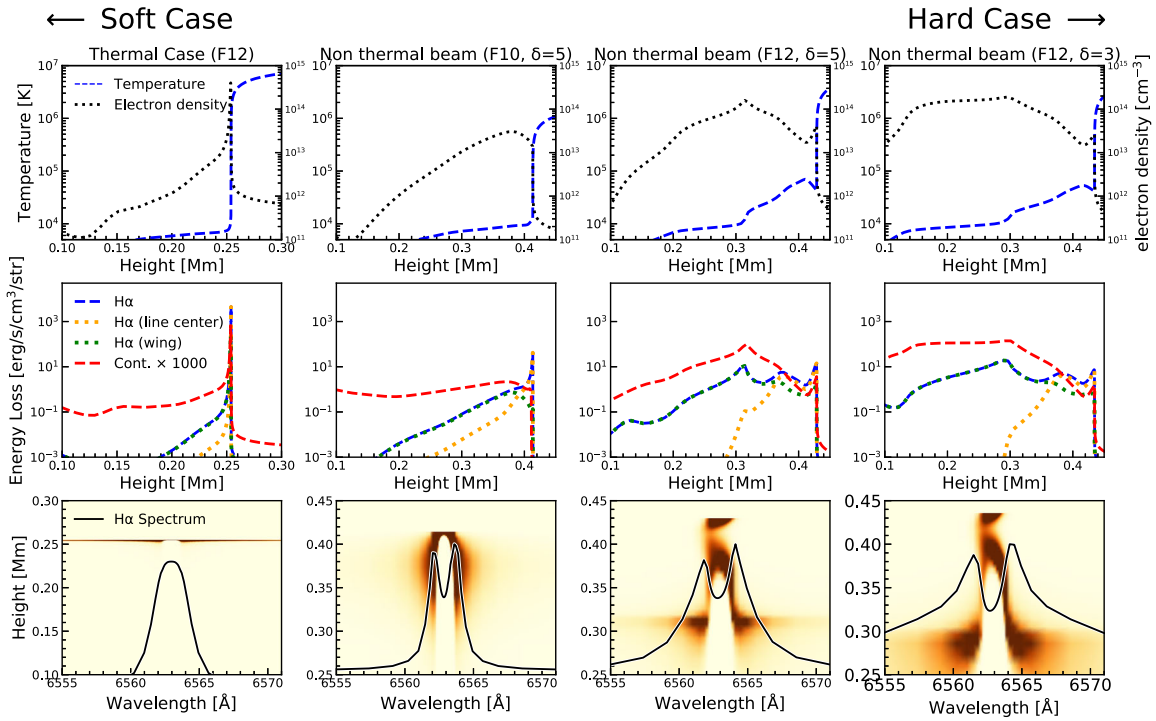

Fig. 10. Examples of the flaring atmospheric condition at the flare peak calculated by the RADYN code for M-type stars. From left to right, soft- to hard-energy input cases are shown. Top: Atmospheric temperature (dashed blue line) and electron density (dotted black line) as functions of height from the photosphere at the flare peak of the Hα radiation. Middle: Contribution functions for Hα and 6690 Å continuum as a function of height. For the Hα, the contribution from line core and wing are plotted separately. Bottom: Background showing the normalized Hα line contribution function in the space of wavelength and atmospheric height. The black curves show the Hα spectra. (Color online)

simulation input parameters. First, we show where the Hα line and continuum emissions come from in the one-dimensional flare atmosphere in figure 10, which shows four typical results for simulated flare atmospheres. The upper panels show the detailed atmospheric structure, the middle panels show the contribution functions of Hα and continuum, and the bottom panels show the line formation region of the Hα. In the middle panels you can see that the Hα (wing and center) and optical continuum enhancements come from the upper to lower chromosphere in the non-thermal electron case (hard case; the right side of figure 10), while they mainly come from the upper chromosphere and transition region in the thermal case (soft case; the left side of figure 10).

Next, let us simply compare the simulated spectra with the observations obtained in section 3. Figure 11 shows a comparison of the Hα spectra between observations and models. For the initial phase (red), the observed line shape is more consistent with the hard- and high-energy spectrum model of F12 ($\delta = 3$). For the later phases, the observed line shape is more consistent with the weaker (F10; $\delta = 3$) or softer (F12; $\delta = 5$) energy spectrum models. Of course, all the observed spectra do not have corresponding "flare peaks" (including the rising/decay phases), and readers may

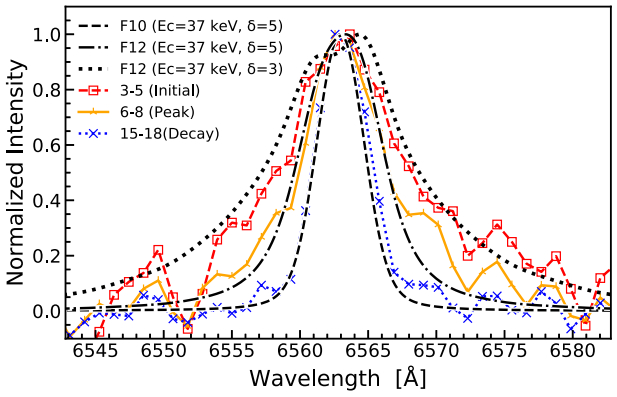

Fig. 11. Comparison of Hα spectra between observations (colored) and model (black). For the observational spectra, the temporal evolution of Hα spectra of flare #1 [panel (B) of figure 3] are plotted. For the model spectra, the F10 ($\delta = 5$), F12 ($\delta = 5$), and F12 ($\delta = 3$) cases are plotted as reference. The model spectra are convolved with the Gaussian instrumental profile of Seimei/KOOLS-IFU ($R \sim 2000$, $\Delta\lambda \sim 3$ Å; Matsubayashi et al. 2019), and the central reversal seen in figure 10 is not resolved in the low-resolution spectra. (Color online)

think that it is better to compare them with time-dependent Hα spectral evolution for a given simulation in a single loop. However, in analogy with solar flares, stellar flares are expected to be observed as a superposition of many

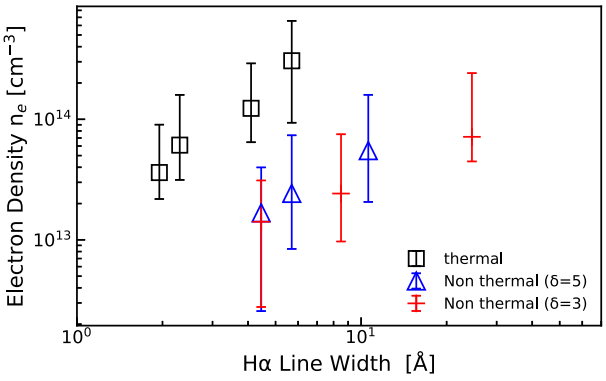

Fig. 12. Comparison between the Hα intensity and electron density weighted by the contribution function of the Hα obtained by the RADYN simulations. The squares show the thermal case. The crosses and triangles show the non-thermal electron cases, and the different symbols indicate the different power-law index. As input energy flux (F#; from F10 to F12) increases, the line width and electron density increase. (Color online)

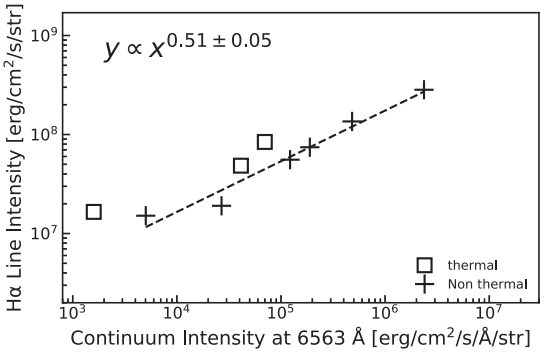

Fig. 13. Comparison between the Hα intensity and continuum intensity at 6563 Å obtained by the RADYN simulations. The Hα intensity is wavelength-integrated across the line. The square symbols show the thermal case, and the cross symbols show the non-thermal electron cases. As input energy flux (F#; from F10 to F12) increases, Hα and continuum intensities increase. The dotted line is the fitted one for the non-thermal case, and the power-law index is derived to be 0.51. Note that the 5F10 thermal case shows very weak continuum emission, and is not plotted in this figure.

magnetic loops, and each footpoint has a different "flare peak." Therefore, under the assumption that one loop quickly decays, the comparison with the peak spectra of each model setup is not so bad, and it is easy to derive the physical parameters of the energy injection. As a result of the comparison between observations and models, one can say that in the initial phase high-energy electrons with large energy deposition rate and hard spectral distribution occurred, and the spectral feature changes to softer/weaker energy injection.

Finally, we show the relation between Hα line broadening and some physical parameters such as atmospheric density or energy injections. Figure 12 shows a comparison between Hα line width and electron density in the chromospheric condensation region at the flare emission peak for each case. For the thermal cases, the emission of Hα is mostly radiated from the upper chromosphere and transition region where there is less self-absorption,[7] so the positive relation for the thermal cases is likely to come from the linear Stark effect (Kowalski et al. 2017). For the non-thermal cases, the harder spectral cases show wider line broadening. If the model atmosphere in F12 ($\delta = 3$) is compared with that in F12 ($\delta = 5$) in figure 10, only the line wing contributions are enhanced in the deep chromosphere for the harder beam of F12 ($\delta = 3$). This would be because the hard high-energy electrons deposited in the deep chromosphere cause a strong Stark effect and self-absorptions. In cases where the electron density is not so different for each case, the self-absorption can largely contribute to these differences.

7 Here, self-absorption means that the emissions are absorbed by the upper atmosphere having such large opacity that they are not able to get to the surface. The upper layer of the chromosphere/transition region (i.e., corona) has very small opacity in the continuum and Balmer lines.

5.4 Simulation result II: Relation between Balmer lines and optical continuum emissions—What are non-white-light flares like?

In this subsection we show the relation between Hα lines and optical continuum emissions as a response to the different kinds of flare simulation input parameters. Figure 13 shows comparisons between the continuum and Hα emission in the RADYN simulations. We found that the relation between the optical continuum and Hα emission is not linear, but expressed as $I_{\mathrm{H}\alpha} \propto I_{\mathrm{cont}}^{\alpha}$, where $\alpha = 0.51 \pm 0.05$. We consider that there are the following possibilities for this nonlinear relation: (1) an opacity difference between optically thick Hα and optically thin continuum in the chromosphere, (2) an emissivity difference between Hα and continuum (e.g., Kowalski et al. 2019), or (3) both.

In the case of possibility (1), since Hα is optically thick in the chromosphere, the line shape heavily suffers from self-absorption, especially in the line center. Therefore, the more energetic the flare input, the less Hα emission ($\eta_{\mathrm{H}\alpha}$) comes from the lower flaring atmosphere compared with the optical continuum, which is optically thin and can escape from a large range of heights. In figure 14, comparisons between the continuum and Hα emission are plotted for the Hα line wing and center separately. You can see that the Hα line center is less sensitive to the flare input and continuum emission. This is because the line center is more optically thick than the line wing, and self-absorption more or less affects the nonlinearity (for the absorption line, see, e.g., figure 9.1 in Rutten 2003).

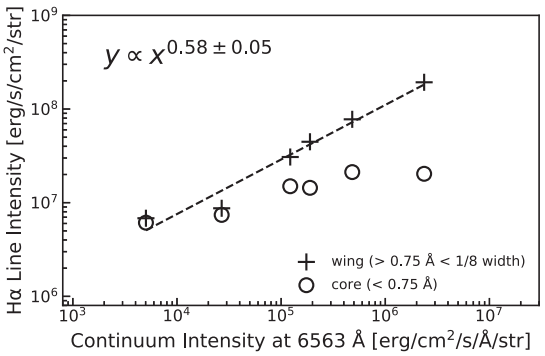

Fig. 14. Comparison between the Hα intensity and continuum intensity at 6563 Å for the non-thermal case obtained by the RADYN simulations. The contribution from line core (circles; <0.75 Å from the line center) and wing (crosses; emission integrated over 0.75 Å from line center to 1/8 width) are separately plotted here. The dotted line is the fitted one for line wing, and the power-law index is derived to be 0.58. As input energy flux (F#; from F10 to F12) increases, Hα and continuum intensities increase. Since the line center is optically thick compared to the line wing, the emergent intensity of line center cannot become large when the input energy becomes large compared to line wing.

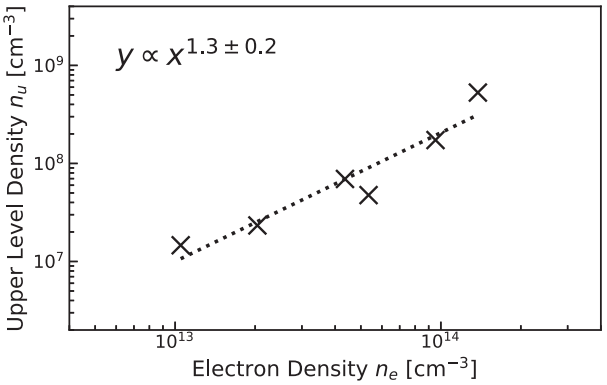

Fig. 15. Comparison between Hα upper-level density and electron density weighted by the line wing contribution function obtained by the RADYN simulations. The dotted line is the fitted one, and the power-law index is derived to be 1.3.

In the case of possibility (2), the emissivity of the Hα can be expressed as

$$\eta_{H\alpha} = \frac{h\nu_0}{4\pi} n_{\rm u} A_{\rm u} \phi(\nu - \nu_0) \propto n_{\rm u}, \quad (1)$$

where $\eta_{H\alpha}$ is the emissivity of Hα, $n_{\rm u}$ is the upper-level hydrogen density ($n = 3$), h is the Planck constant, ν_0 is the line center frequency, $A_{\rm u}$ is the Einstein constant, and ϕ is the profile function for Hα. On the other hand, the emissivity of the optical continuum ($\eta_{\rm cont}$) can be expressed as

$$\eta_{\rm cont.} = n_{\rm e} n_{\rm p} F(T, \nu) \propto n_{\rm e}^2, \quad (2)$$

where $n_{\rm e}$ is the electron density, $n_{\rm p}$ is the proton density, and $F(T, \nu)$ is a function of temperature T and frequency ν (for the detailed expression, see Kowalski et al. 2019), if we assume the Paschen continuum is dominant in the optical range. If we assume that the electron density is roughly proportional to the upper-level density of Hα and the temperature is not so different in the chromospheric layers, we can deduce $\eta_{\rm H\alpha} \propto \eta_{\rm cont}^{\alpha}$, where $\alpha \sim 0.5$, which may be able to explain the non-linearity. Figure 15 shows a comparison between $n_{\rm e}$ and $n_{\rm u}$, weighted by the continuum and line-wing contribution function, respectively. Considering the obtained relation $n_{\rm u} \propto n_{\rm e}^{1.3 \pm 0.2}$, the equations (1) and (2) reduce to $I_{\rm H\alpha} \propto I_{\rm cont}^{\alpha}$, where $\alpha \sim 0.65$ (with $\tau_{\rm wing} \ll 1$ in the chromosphere), which is similar to the relations for the line wing: $I_{\rm H\alpha wing} \propto I_{\rm cont}^{\alpha}$, where $\alpha = 0.58 \pm 0.05$.

These results mean that the non-linear relation between Hα and the continuum intensity comes from both (1) the opacity effect and (2) the emissivity difference. This non-linearity means that the emergent continuum intensity more significantly decreases than the emergent Hα intensity when the energy input rate into the chromosphere decreases. For example, the Hα intensity decreases by a factor of 3, whereas the continuum intensity decreases by one order of magnitude. This can explain why there is no white-light emission on the relatively weak Hα flares: white-light emission is difficult to detect compared to the Hα emission in the case of weak flares.

6 Discussion and conclusion

6.1 Stellar flares: Observations and simulations

Let us summarize the observational results in this work. We performed monitoring observations on an M-dwarf flare star AD Leo during 8.5 nights with the Seimei Telescope, SCAT, and NICER, with the collaboration of the OISTER program. Twelve flares were detected, and multi-wavelength data were obtained for several flares (see section 3 and the Appendix). In particular, flare #1 was a superflare with energy 1.4×10^{33} erg in the g'-band filter (the total radiated energy in all the optical filters was 1.9×10^{33} erg). We found the following three interesting events:

(1) During the superflare (flare #1), the Hα emission line full width at 1/8 maximum dramatically increases to 14 Å from 8 Å, accompanied by large white-light flares (subsection 3.2).
(2) Some weak Hα and X-ray flares (e.g., flare #4) are not accompanied by white-light emissions; these are candidates for so-called non-white-light flares in the case of solar flares (subsection 3.4).
(3) Clear rotational modulations are found in X-ray/Hα in the same phase, whereas the continuum periodicity is

not clear due to the photometric sensitivity (section 4; discussed in subsection 6.2).

We performed a one-dimensional RHD simulation with the RADYN code to understand the behavior of the Hα and optical continuum obtained in points (1) and (2) above (section 5).

For point (1), the numerical simulation (subsection 5.3) shows that the line width of Hα largely depends on both the energy flux density (F) and the energy spectrum (a power-law index δ). By changing the energy spectra, the degree of contribution from Stark broadening and opacity broadening does change, meaning that it is difficult to constrain the input energy spectra from only the Hα spectra of the superflare, flare #1. Even if the additional information such as the continuum fluxes is given, there is another degeneracy between intensity (I) and emission area ($A_{\rm flare}$), which makes it difficult to constrain the energy spectra.

Considering the large Hα broadening during the superflare, it would be at least possible to say that the Hα broadening in the initial phase of the superflare indicates a hard and/or high-energy flare injection via non-thermal electrons, like the case with $F_{\rm NT} = 10^{12}\,{\rm erg\,cm^{-2}\,s^{-1}}$ and $\delta = 3$, and the decrease in the line width indicates the decrease of the energy flux density and/or the softening of energy spectra at different locations in the flare ribbon. Previous studies also indicate that $F_{\rm NT} = 10^{12}\,{\rm erg\,cm^{-2}\,s^{-1}}$ (low-energy cutoff $\gg$37 keV) or $10^{13}\,{\rm erg\,cm^{-2}\,s^{-1}}$ is necessary to reproduce the broad-band continua of M-dwarf flares (Kowalski et al. 2016), and fluxes larger than this are sometimes inferred even on the Sun (Krucker et al. 2011). More comparisons between observations and models can give us a clue to the universality or difference of the particle acceleration on solar and stellar flares.

For point (2), our simulation also shows that the Hα and optical continuum intensity have a non-linear relation $I_{\rm H\alpha} \propto I_{\rm cont}^{\alpha}$, where $\alpha \sim 0.5$, which is largely caused by the opacity and emissivity difference (subsection 5.4). This non-linearity can contribute to the cause of non-white-light flares: as the energy input rates decrease, the continuum emissions decrease more significantly than the Hα emissions. In the case of a solar flare, it is reported that non-white-light flares tend to have long durations, i.e., small energy deposition rates (Canfield & Gayley 1987; Matthews et al. 2003; Watanabe et al. 2017), which is consistent with our simulation and interpretation/analysis. However, it would not be consistent with the relatively short duration of $\sim$7 min of flare #4, and we need more samples of stellar non-white-light events (e.g., H. Maehara et al. in preparation), and validation in spatially resolved solar flares would be required. As another possibility, stellar non-white-light flares may be explained by a flare over the limb. In this case, if we assume that white-light emissions originate from only the chromosphere/photosphere, like solar flares, the white-light emission source at loop footpoints is invisible while the X-ray and Hα emission are visible in the flare loop in the corona. However, this possibility may be less likely because white-light emissions can be visibly emitted from the dense (post) flare loops (Heinzel & Shibata 2018; Jejčič et al. 2018) even though the footpoints are invisible over the stellar limb.

6.2 Rotational modulations

As summarized in point (3) of subsection 6.1, we found X-ray and Hα rotational modulations on AD Leo with a period of 2.24 d in almost the same phase (see section 4). It is, to our knowledge, rare to simultaneously detect rotational modulation in coronal and chromospheric emissions on M-dwarf stars, although some previous studies have shown rotational modulations with broad-band optical and X-ray (Wargelin et al. 2017) or with only X-ray (e.g., Marino et al. 2003; Hussain et al. 2007). The correlation between chromospheric and coronal emission would be because both Hα and X-ray would come from the magnetically active regions. Although the small difference of rotational phase ($\sim$0.1) between Hα and X-ray may indicate a difference in the visibility or location of the bright active region at each wavelength, it may be due to the sparse data sampling and/or the very rough fitting by a sine curve. The amplitude of the brightness variation in X-ray and Hα is 32% and 16%, respectively. The factor-of-two difference in amplitude between X-ray and Hα may be due to the difference in the active region filling factor between chromosphere and corona, but may be due to the contrast between the active region and quiet regions. Saar and Linsky (1985), however, inferred that 73% of the surface of AD Leo is covered by active regions outside of dark spots. One possibility to explain the difference between the observed brightness amplitude in X-ray/Hα and the reported filling factor is that the low inclination angle of AD Leo ($i = 20^{\circ}$; Morin et al. 2008) reduces the brightness amplitude, and the other is that the large filling factor significantly reduces the stellar brightness amplitude (Eker 1994; Schrijver 2020).

Although rotational brightness variations were detected for X-ray, we could not detect clear rotational variations in the hardness ratio of the X-ray band related to the coronal temperature: the spectra show a relatively low hardness ratio even in high X-ray intensity. This could be because the temperature is not sensitive to the magnetic loop size (Rosner et al. 1978), or may be because the active region consists of a group of small magnetic loops and therefore the increase in the number of magnetic loops does not affect the changes in coronal temperature.

The optical rotational modulation is less than ~6%, possibly due to the lack of sensitivity, but maybe it is true considering that the optical variability of M dwarfs like GJ 1243 (dMe4.0V) is comparable with this amplitude in Kepler (e.g., Hawley et al. 2014; Davenport et al. 2014). However, considering this low inclination angle, the *I*-band amplitude of 6% looks rather large, and it would be interesting to try photometric spot modeling on the data (e.g., Namekata et al. 2020). The optical rotational phase is not completely anti-correlated with the X-ray/Hα ones (0.2–0.3 rotational phase), which may indicate that the spotted side of the hemisphere is not the same as the coronal/chromospheric active regions, although more precise measurements of the optical rotational modulation would be necessary to draw conclusions. In this observational period, it is difficult to estimate the active region emergence or decay, but long-term continuous multi-wavelength monitoring observation can reveal the signature of magnetic flux emergence/decay in the stellar chromosphere/coronae (e.g., Namekata et al. 2019, 2020)

6.3 Future work

Finally, we introduce our plan for the Seimei–OISTER campaign. We will continue the flare monitoring of M-dwarf flare stars with the Seime–OISTER campaign to obtain statistical samples. In 2018, Transiting Exoplanet Survey Satellite (TESS; Ricker et al. 2015) was launched and has begun to provide us midterm (27 d–1 yr) stellar photometric data of nearby stars, including flare stars. This would be a good opportunity to do the long-sought simultaneous observation of stellar flares as well as rotational modulations with high-sensitivity space-based photometry, ground-based and X-ray telescope, which will open new doors for stellar flare study. Also, we could not detect the line asymmetry of the Hα lines, but whether symmetry/asymmetry is common should be investigated in future work because it may be related to stellar coronal mass ejections (e.g., Vida et al. 2016, 2019; Honda et al. 2018; Fuhrmeister et al. 2018). Moreover, the measurement of the optical spectra for superflares on G-type main-sequence stars (e.g., Maehara et al. 2012; Notsu et al. 2019) is still challenging but will be tried by combining TESS with our ground-based observations, which would have an impact on our understanding of stellar extreme events.

Acknowledgment

This work was supported by JSPS KAKENHI Grant Numbers JP16H03955 (K.S.), JP17H02865 (D.N.), JP17K05400 (M.H.), JP17J08772 (M.K.), JP17K05392 (Y.T.), and JP18J20048 (K.N.). K.N. is supported by the JSPS Overseas Challenge Program for Young Researchers. Y.N. is supported by the JSPS Overseas Fellowship Program. Y.N. also acknowledge the International Space Science Institute and the supported International Team 464: The Role Of Solar And Stellar Energetic Particles On (Exo)Planetary Habitability (ETERNAL, http://www.issibern.ch/teams/exoeternal/). This work was also supported by the Optical and Near-infrared Astronomy Inter-University Cooperation Program and Grants-in-Aid of the Ministry of Education.

Appendix. Flare atlas

In this appendix we will show the observed flares that are not discussed in the main part of this paper but are important for our future studies. Figure 16 shows the light curves observed with the 40 cm KU (Kyoto University) Telescope (*B*-band photometry), Seimei Telescope, and NICER on 2019 April 12. Five small but clear flares are detected in this period (see flares #7–#11).

Figure 17 shows the light curves observed with only NICER on 2019 April 13. We estimated the emission measure and temperature of flare #12, and it is found that the peak timing of the temperature is similar to that of the emission measure. The flare energy in X-ray (0.5–10 keV) is estimated to be 9.7×10^{31} erg, which is very large and comparable to the largest scale of solar flares.

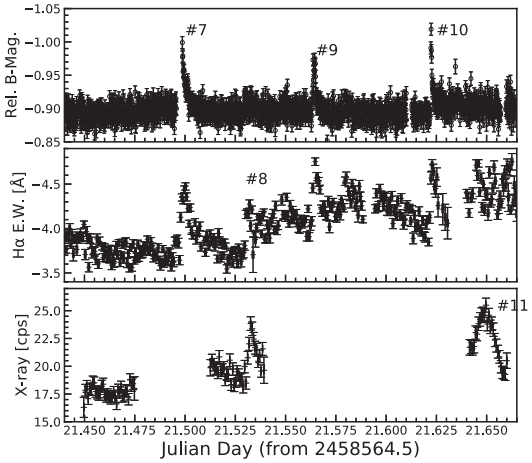

Fig. 16. *B*-band, Hα, X-ray light curve during 2019 April 12. The detected flares #7–#11 are labeled.

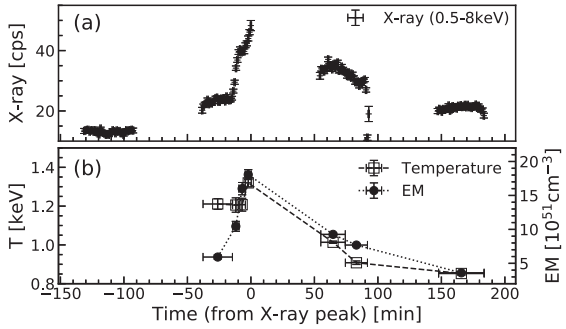

Fig. 17. X-ray large flares (SF #12) detected only with NICER. Panel (a) shows the X-ray light curve (0.5–8.0 keV). Panel (b) shows the temporal evolution of emission measure and temperature. The radiated energy in the 0.5–10 keV band is estimated to be 9.7×10^{31} erg.

References

Airapetian, V. S., Glocer, A., Gronoff, G., Hébrard, E., & Danchi, W. 2016, Nature Geosci., 9, 452

Allred, J. C., Hawley, S. L., Abbett, W. P., & Carlsson, M. 2005, ApJ, 630, 573

Allred, J. C., Hawley, S. L., Abbett, W. P., & Carlsson, M. 2006, ApJ, 644, 484

Allred, J. C., Kowalski, A. F., & Carlsson, M. 2015, ApJ, 809, 104

Aulanier, G., Démoulin, P., Schrijver, C. J., Janvier, M., Pariat, E., & Schmieder, B. 2013, A&A, 549, A66

Benz, A. O., & Güdel, M. 2010, ARA&A, 48, 241

Canfield, R. C., & Gayley, K. G. 1987, ApJ, 322, 999

Carlsson, M., & Stein, R. F. 1992, ApJ, 397, L59

Carlsson, M., & Stein, R. F. 1995, ApJ, 440, L29

Carlsson, M., & Stein, R. F. 1997, ApJ, 481, 500

Carlsson, M., & Stein, R. F. 2002, ApJ, 572, 626

Crespo-Chacón, I., Montes, D., García-Alvarez, D., Fernández-Figueroa, M. J., López-Santiago, J., & Foing, B. H. 2006, A&A, 452, 987

Davenport, J. R. A., et al. 2014, ApJ, 797, 122

Eker, Z. 1994, ApJ, 420, 373

Fisher, G. H. 1989, ApJ, 346, 1019

Fuhrmeister, B., et al. 2018, A&A, 615, A14

Fuhrmeister, B., Lalitha, S., Poppenhaeger, K., Rudolf, N., Liefke, C., Reiners, A., Schmitt, J. H. M. M., & Ness, J.-U. 2011, A&A, 534, A133

Gendreau, K. C., et al. 2016, SPIE Proc., 9905, 99051H

Graham, D. R., Cauzzi, G., Zangrilli, L., Kowalski, A., Simões, P., & Allred, J. 2020, arXiv:2004.05075

Hawley, S. L., et al. 1995, ApJ, 453, 464

Hawley, S. L., et al. 2003, ApJ, 597, 535

Hawley, S. L., Davenport, J. R. A., Kowalski, A. F., Wisniewski, J. P., Hebb, L., Deitrick, R., & Hilton, E. J. 2014, ApJ, 797, 121

Hawley, S. L., & Pettersen, B. R. 1991, ApJ, 378, 725

Hayakawa, H., et al. 2017, ApJ, 850, L31

Heinzel, P., & Shibata, K. 2018, ApJ, 859, 143

Holman, G. D., Sui, L., Schwartz, R. A., & Emslie, A. G. 2003, ApJ, 595, L97

Honda, S., Notsu, Y., Namekata, K., Notsu, S., Maehara, H., Ikuta, K., Nogami, D., & Shibata, K. 2018, PASJ, 70, 62

Hori, K., Yokoyama, T., Kosugi, T., & Shibata, K. 1997, ApJ, 489, 426

Hunt-Walker, N. M., Hilton, E. J., Kowalski, A. F., Hawley, S. L., & Matthews, J. M. 2012, PASP, 124, 545

Hussain, G. A. J., et al. 2007, MNRAS, 377, 1488

Ichimoto, K., & Kurokawa, H. 1984, Sol. Phys., 93, 105

Ježič, S., Kleint, L., & Heinzel, P. 2018, ApJ, 867, 134

Kahler, S., et al. 1982, ApJ, 252, 239

Kotani, T., et al. 2005, Nuovo Cim. C, 28, 755

Kowalski, A. F., et al. 2017, ApJ, 837, 125

Kowalski, A. F., Butler, E., Daw, A. N., Fletcher, L., Allred, J. C., De Pontieu, B., Kerr, G. S., & Cauzzi, G. 2019, ApJ, 878, 135

Kowalski, A. F., Hawley, S. L., Carlsson, M., Allred, J. C., Uitenbroek, H., Osten, R. A., & Holman, G. 2015, Sol. Phys., 290, 3487

Kowalski, A. F., Hawley, S. L., Wisniewski, J. P., Osten, R. A., Hilton, E. J., Holtzman, J. A., Schmidt, S. J., & Davenport, J. R. A. 2013, ApJS, 207, 15

Kowalski, A. F., Mathioudakis, M., Hawley, S. L., Wisniewski, J. P., Dhillon, V. S., Marsh, T. R., Hilton, E. J., & Brown, B. P. 2016, ApJ, 820, 95

Koyama, K., Hamaguchi, K., Ueno, S., Kobayashi, N., & Feigelson, E. D. 1996, PASJ, 48, L87

Krucker, S., Hudson, H. S., Jeffrey, N. L. S., Battaglia, M., Kontar, E. P., Benz, A. O., Csillaghy, A., & Lin, R. P. 2011, ApJ, 739, 96

Kurita, M., et al. 2020, PASJ, 72, 48

Lingam, M., & Loeb, A. 2017, ApJ, 848, 41

Maehara, H., et al. 2012, Nature, 485, 478

Maehara, H., Notsu, Y., Notsu, S., Namekata, K., Honda, S., Ishii, T. T., Nogami, D., & Shibata, K. 2017, PASJ, 69, 41

Marino, A., Micela, G., Peres, G., & Sciortino, S. 2003, A&A, 407, L63

Matsubayashi, K., et al. 2019, PASJ, 71, 102

Matthews, S. A., van Driel-Gesztelyi, L., Hudson, H. S., & Nitta, N. V. 2003, A&A, 409, 1107

Morin, J., et al. 2008, MNRAS, 390, 567

Muheki, P., Guenther, E. W., Mutabazi, T., & Jurua, E. 2020, A&A, 637, A13

Namekata, K., et al. 2017, ApJ, 851, 91

Namekata, K., et al. 2019, ApJ, 871, 187

Namekata, K., et al. 2020, ApJ, 891, 103

Neupert, W. M. 1968, ApJ, 153, L59

Notsu, Y., et al. 2019, ApJ, 876, 58

Osten, R. A., Hawley, S. L., Allred, J., Johns-Krull, C. M., Brown, A., & Harper, G. M. 2006, ApJ, 647, 1349

Paulson, D. B., Allred, J. C., Anderson, R. B., Hawley, S. L., Cochran, W. D., & Yelda, S. 2006, PASP, 118, 227

Pettersen, B. R., Coleman, L. A., & Evans, D. S. 1984, ApJS, 54, 375

Priest, E. R. 1981, Solar Flare Magnetohydrodynamics (New York: Gordon and Breach Science Publishers)

Ricker, G. R., et al. 2015, J. Astron. Telesc., Instrum., Syst., 1, 014003

Rosner, R., Tucker, W. H., & Vaiana, G. S. 1978, ApJ, 220, 643

Rutten, R. J. 2003, Radiative Transfer in Stellar Atmospheres (Utrecht: Utrech University)

Saar, S. H., & Linsky, J. L. 1985, ApJ, 299, L47

Schrijver, C. J. 2020, ApJ, 890, 121

Segura, A., Walkowicz, L. M., Meadows, V., Kasting, J., & Hawley, S. 2010, Astrobiology, 10, 751

Shibata, K., et al. 2013, PASJ, 65, 49

Shibata, K., & Magara, T. 2011, Living Rev. Solar Phys., 8, 6

Shibata, K., & Yokoyama, T. 2002, ApJ, 577, 422

Shkolnik, E., Liu, M. C., & Reid, I. N. 2009, ApJ, 699, 649

Tei, A., et al. 2018, PASJ, 70, 100

Tremblay, P.-E., & Bergeron, P. 2009, ApJ, 696, 1755

Tsuboi, Y., et al. 2016, PASJ, 68, 90

Vida, K., et al. 2016, A&A, 590, A11

Vida, K., Leitzinger, M., Kriskovics, L., Seli, B., Odert, P., Kovács, O. E., Korhonen, H., & van Driel-Gesztelyi, L. 2019, A&A, 623, A49

Wargelin, B. J., Saar, S. H., Pojmański, G., Drake, J. J., & Kashyap, V. L. 2017, MNRAS, 464, 3281

Warren, H. P. 2006, ApJ, 637, 522

Watanabe, K., Kitagawa, J., & Masuda, S. 2017, ApJ, 850, 204